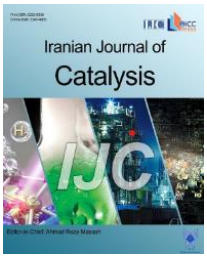

Iran. J. Catal. 2026; 16(2): 299-314

Iranian Journal of Catalysis (IJC)

https://doi.org/10.57647/ijc.2026.1602.19

Research Article

Preparation and Characterization of Visible-Light-driven Sm-doped Bi_2MoO_6 Photocatalyst Used for Enhanced Degradation of Rhodamine B

Anukorn Phuruangrat[1,*], Yothin Chimupala[2], Budsabong Kuntalue[3], Titipun Thongtem[4,5] , Somchai Thongtem[4,6,*]

[1]*Division of Physical Science, Faculty of Science, Prince of Songkla University, Hat Yai, Songkhla 90112, Thailand*
[2] *Department of Industrial Chemistry, Faculty of Science, Chiang Mai University, Chiang Mai 50200, Thailand*
[3]*Advanced Scientific Instruments Unit (ASci Unit), Faculty of Science,Chiang Mai University, Chiang Mai 50200, Thailand*
[4] *Materials Science Research Center, Faculty of Science, Chiang Mai University, Chiang Mai 50200, Thailand*
[5]*Department of Chemistry, Faculty of Science, Chiang Mai University, Chiang Mai 50200, Thailand*
[6] *Department of Physics and Materials Science, Faculty of Science, Chiang Mai University, Chiang Mai 50200, Thailand*

* **Corresponding authors:** phuruangrat@hotmail.com, schthongtem@yahoo.com

Article History:

Received:
26 November 2025

Revised:
11 January 2026

Accepted:
01 February 2026

Published Online:
11 May 2026

Published in Issue:
30 June 2026

Abstract

Bi_2MoO_6 samples containing different weight contents of Sm dopant as the visible-light-driven photocatalyst were successfully synthesized by hydrothermal method. All of them were certified as orthorhombic Bi_2MoO_6 nanoplates. The visible-light absorption range of Bi_2MoO_6 was increased by increasing in the Sm dopant. Different weight contents of Sm dopant containing in Bi_2MoO_6 were studied through the degradation of rhodamine B (RhB) under visible light irradiation. The photocatalytic efficiency of 1% Sm doped-Bi_2MoO_6 nanoplates was the highest of 96.27% or 3.91 times of Bi_2MoO_6 (24.65%) by increasing specific surface area, visible light harvest and separation of charge carriers.

Keywords: Active radicals; Photocatalysis; Photocatalytic mechanism; Sm-doped Bi_2MoO_6

Cite this article: A. Phuruangrat, Y. Chimupala, B. Kuntalue, T. Thongtem, S. Thongtem, Iran. J. Catal. **16** (2026) 299-314.
https://doi.org/10.57647/ijc.2026.1602.19

1. Introduction

In recent decades, the metal oxide semiconductor has an interesting potential for environmental treatment of pollutants released from textile, paper, cosmetic, plastic and rubber industries because it is very effective, non-toxic and environmental friendliness, and has low energy consumption without secondary pollution synthesis [1-6]. Specifically, rhodamine B (RhB) as xanthene cationic dye is extensively used in textile, paper, leather and plastic industries and drained into water reservoirs without treatment [7-9].

It is highly toxic to various aquatic organisms. It has influence on the metabolic and physiological, potentially

carcinogenic, mutagenic and neurotoxic processes to humans and animals, including the cause of skin irritation, eyes and respiratory system [7, 8, 10]. Under light irradiation, the metal oxide semiconductor can lead to produce active species used to oxidize toxic organic pollutants during photocatalytic reaction [3, 4, 11-13]. TiO_2 is a traditional semiconductor photocatalyst for environmental purification because of its inexpensiveness, highly performance activity, stable chemical and physical material, and non-toxicity [14, 15]. Nevertheless, TiO_2 with a wide band gap of 3.2 eV is only responsive to the ultraviolet (UV) light with only ~4% of the solar spectrum for photodegradation of organic pollutants [1, 14-17]. Therefore, the visible-light-driven photocatalyst has been studied in recent years for utilization of solar energy with high efficiency.

Bismuth molybdate (Bi_2MoO_6) as a narrow bandgap of 2.5–2.8 eV has a layered Aurivillius structure which consists of perovskite $(MoO_4)^{2-}$ layers sandwiched between $(Bi_2O_2)^{2+}$ layers. It is one of the most promising visible-light-driven photocatalytic materials with its non-toxic property, high chemical stability and suitable VB and CB edge for redox reaction [18-22]. Bi_2MoO_6 has a photocatalytic activity for removing Cr(VI) [19, 23], reduction of CO_2 [20, 24], water splitting [21, 22] and organic pollutant degradation [23, 25, 26]. Bi_2MoO_6 was synthesized by many researchers. For example, Xie et al. succeeded in synthesizing flake-like nanoscale Bi_2MoO_6 powder by a simple low-temperature molten salt method [25]. Bi_2MoO_6 is good in photocatalysis of rhodamine B (RhB) degradation at room temperature. It is an active oxygen donor in photo-oxidation process and improvement its photocatalytic activity. Cruz et al. reported the preparation of γ-Bi_2MoO_6 by co-precipitation method with 450 °C calcination following behind. The research showed the degradation of rhodamine B (RhB), indigo carmine (IC) and methyl orange (MO) under visible light irradiation [26]. Although Bi_2MoO_6 has excellent performance in separating charge carriers, high recombination rate of photogenerated charge carriers also limited its photocatalytic activity and practical application [18-20, 22, 23].

The previous studies reported the strategies to improve photocatalytic performance of Bi_2MoO_6 such as morphology modification [27, 28], anion doping [29, 30], cation doping [31-33], construction of heterojunction [34, 35], metal loading [36-38] and surface medication [39, 40]. Among them, cation doping is the promising method to improve visible light driven photocatalytic performance of Bi_2MoO_6 by increasing light absorption capacity, narrowing band gap and carrier separation by forming oxygen vacancies inside [31, 32, 41]. For example, Qiu et al. succeeded in synthesizing a series of visible-light-driven 0.05-3.0% Y^{3+}-doped B_2MoO_6 photocatalysts by a hydrothermal method [31]. They found that 1.5% Y-doped Bi_2MoO_6 showed the highest degradation of rhodamine B (RhB) and Congo red (CR) organic pollutants under visible light irradiation because Yb^{3+} dopant was able to greatly promote the diffusion and separation of photoexcited carriers containing inside. Yu et al. reported that Gd^{3+} doped Bi_2MoO_6 nanoplates showed excellent photodegradation of RhB under visible light irradiation because Gd^{3+} dopant has the influence to improve visible light harvest and promote the separation of photogenerated electrons and holes containing in Bi_2MoO_6 [41]. Among different rare earth metals, Sm^{3+} dopant with incompletely occupied 4f orbitals and empty 5d orbitals played the role in improving the photocatalytic performance. Thus, Sm^{3+} dopant has the ability to promote the efficient separation of photoinduced electron-hole pairs and enhance photocatalytic reaction [32, 42-44]. Zhang et al. succeeded in synthesizing of $Sm_xBi_{2-x}WO_6$ (x = 0.0%, 0.5%, 1.0%, 2.0) by a hydrothermal method [43]. The $Sm_{0.01}Bi_{1.99}WO_6$ has the highest activity for RhB degradation caused by the synergistic effect of appropriate band gap and high specific surface area of Sm-doped Bi_2MoO_6. Upon being doped with Sm, $BiVO_4$ played a role in enhancing the photodegradation of methylene blue (MB) because the dopant has the influence to enhance efficient separation of electron–hole pairs [44].

The as-synthesized visible-light-driven Sm-doped Bi_2MoO_6 nanoplates were characterized by X-ray diffraction (XRD), Raman and Fourier transform infrared (FTIR) spectrometry, scanning electron and transmission electron microscopy (SEM and TEM) and X-ray photoelectron spectrometry (XPS). The optical properties and surface area of visible-light-driven Sm-doped Bi_2MoO_6 nanoplates were investigated by ultraviolet-visible absorption spectroscopy and nitrogen adsorption–desorption surface area analysis. The visible-light-driven Sm-doped Bi_2MoO_6 nanoplates were tested for the degradation of RhB under visible light irradiation. The effect of different weight contents of Sm dopant was studied through RhB degradation under visible light irradiation and discussed according to the experimental results.

2. Experimental

To synthesize Sm-doped Bi_2MoO_6 nanoplates, 0.01 mole of bismuth (III) nitrate pentahydrate ($Bi(NO_3)_3{\cdot}5H_2O$) and 0.005 mole of sodium molybdate dihydrate ($Na_2MoO_4{\cdot}2H_2O$) were dissolved in 80 ml distilled with being stirred to form suspension solution. Concurrently, 0–2% by weight of samarium (III) nitrate hexahydrate ($Sm(NO_3)_3{\cdot}6H_2O$) dissolved in 20 ml distilled water was added into the mixed suspension solution with being stirred at the room temperature behind. The mixture was adjusted the pH to 6 by 3 M sodium hydroxide (NaOH) and put in a 200 ml home-made Teflon-lined stainless-

10.57647/ijc.2026.1602.19

steel autoclave. The hydrothermal reactor was sealed and heated in an electric oven at 180 ºC for 20 h. At the end of hydrothermal process, the as-synthesized Sm-doped Bi_2MoO_6 was filtered by Whatman filter paper no 5, washed with distilled water and 95% ethanol to remove inorganic residues and dried at 80 ºC for 12 h.

Phase and crystallinity of the samples were characterized by a Philips X'Pert MPD X-ray diffractometer (XRD). The atomic vibration of samples was studied using a BRUKER TENSOR 27 Fourier transform infrared (FTIR) spectrometer and a HORIBA JOBIN YVON T64000 Raman spectrometer with 50 mW and 514.5 nm wavelength Ar green laser. The morphologies of Sm-doped Bi_2MoO_6 were examined using scanning electron microscopy (SEM, JEOL JSM IT800) at an accelerating voltage of 35 kV combined with an Oxford Instruments Energy-Dispersive Spectroscopy (EDS) and transmission electron microscopy (TEM, JEOL JEM-2010) at an accelerating voltage of 200 kV. The oxidation states of elements and elemental composition of Sm-doped Bi_2MoO_6 were analyzed by an X-ray photoelectron spectrometer (XPS) Kratos Axis Ultra DLD using monochromates Al K_α radiation at 1486.6 eV and C 1s at 285.1 eV as a standard. The surface area and pore size of Sm-doped Bi_2MoO_6 were analyzed through nitrogen adsorption–desorption isotherms by a Micromeritics ASAP 2020 surface area analyzer at 77 K. The optical absorption of Sm-doped Bi_2MoO_6 was analyzed by Shimadzu UV-2600 UV-visible absorption spectroscopy at 200–800 nm wavelength.

Photocatalytic activities of Bi_2MoO_6 containing different weight contents of Sm dopant were monitored by rhodamine B (RhB) degradation under visible light illumination from a 35 W xenon lamp with a 420 nm cutoff filter. Each 0.2 g of Bi_2MoO_6 containing different weight contents of Sm dopant was put in 200 ml of $1x10^{-5}$ M RhB solutions which were magnetically stirred in the dark for 30 min. Subsequently, the solution system was irradiated by visible light of the xenon lamp and was collected for 5 ml every 30 min interval. The sampled solution was centrifuged at 4500 rpm for 10 min and was determined the content of RhB at the maximum absorption wavelength (λ_{max}) of 554 nm by Lambda 25 UV–visible spectroscopy, PerkinElmer Inc. The decolorization efficiency can be calculated by the following.

$$\text{Decolorization efficiency (\%)} = \frac{C_o - C_t}{C_o} \times 100 \quad (1)$$

C_o and C_t are the concentrations of RhB at time t = 0 and after light irradiation for a period of time (t). The degradation pathway of RhB photocatalyzed by 1% Sm-doped Bi_2MoO_6 under visible light irradiation for t = 0, 90 and 150 min was investigated by a liquid chromatograph-quadrupole time-of-flight mass spectrometer (LC-QTOF MS), 1290 infinity II LC-6545 quadrupole-TOF, Agilent Technologies, using a positive electrospray ionization (ESI^+) mode.

3. Results and discussion

The crystal structure and phase of as-prepared samples were investigated by XRD (Fig. 1). XRD pattern of Bi_2MoO_6 prepared by the hydrothermal method at 180 ºC for 20 h shows the dominant diffraction peaks at 2θ of 10.96º, 23.59º, 28.29º, 32.65º, 33.15º, 36.10º, 46.78º, 47.17º, 55.56º, 56.32º and 58.50º which were respectively assigned to the (020), (111), (131), (002), (060), (151), (202), (062), (331), (082) and (262) crystallographic planes of orthorhombic Bi_2MoO_6 structure (JCPDS no. 00-021-0102 [45]). Upon the introduction of Sm into Bi_2MoO_6, XRD patterns of Sm-doped Bi_2MoO_6 can be indexed to orthorhombic Bi_2MoO_6 structure (JCPDS no. 00-021-0102 [45]). The crystal structure and phase of the samples were not changed although Sm dopant was introduced into Bi_2MoO_6 lattice. However, the diffraction peaks of Bi_2MoO_6 became border and weaker by the introduction of Sm dopant. Thus, the crystallite size and crystalline degree of Sm-doped Bi_2MoO_6 were decreased. The (131) crystallographic plane of Bi_2MoO_6 was slightly shifted to higher angle because the ionic radius of Bi^{3+} (1.03 Å [16, 30, 33, 43]) is larger than the ionic radius of Sm^{3+} (0.958 Å [43, 46, 47]). This result indicated that Sm^{3+} ions substituted for Bi^{3+} ions of Bi_2MoO_6 lattice. The distorted orthorhombic Bi_2MoO_6 structure led to defect formation inside [48-50]. The approximate particle sizes calculated by Scherrer equation [41, 43, 51, 52] are shown in Table 1. The particle sizes of Bi_2MoO_6 were decreased with increasing in the loaded Sm dopant because they were suppressed by defects inside [16, 31, 32]. Moreover, the calculated cell parameters and volumes of Bi_2MoO_6 are summarized in Table 1 [43, 53, 54]. They were also decreased with increasing in the loaded Sm. These were certified as the substitution of Sm^{3+} ions for Bi^{3+} ions of Bi_2MoO_6 lattice.

Fig. 2a shows the FTIR spectra of as-prepared samples. They show the characteristic broad band at 3200–3400 cm^{-1} which are attributed to the stretching vibration of O–H bond belonging to water molecules adsorbed on the surface of as-prepared samples [1, 3, 4, 15, 16, 29].

The small FTIR peaks at 446 and 575 cm^{-1} of pure Bi_2MoO_6 sample were detected and were attributed to the vibration of Bi–O bond of BiO_6 and bending vibration of $[MoO_6]^{6-}$ [1, 3, 4, 15, 16, 29]. The dominant FTIR peak at 736 cm^{-1} was attributed to the asymmetric stretching of equatorial oxygen atoms containing in $[MoO_6]^{6-}$ octahedrons [1, 3, 4, 15, 16, 29].

10.57647/ijc.2026.1602.19

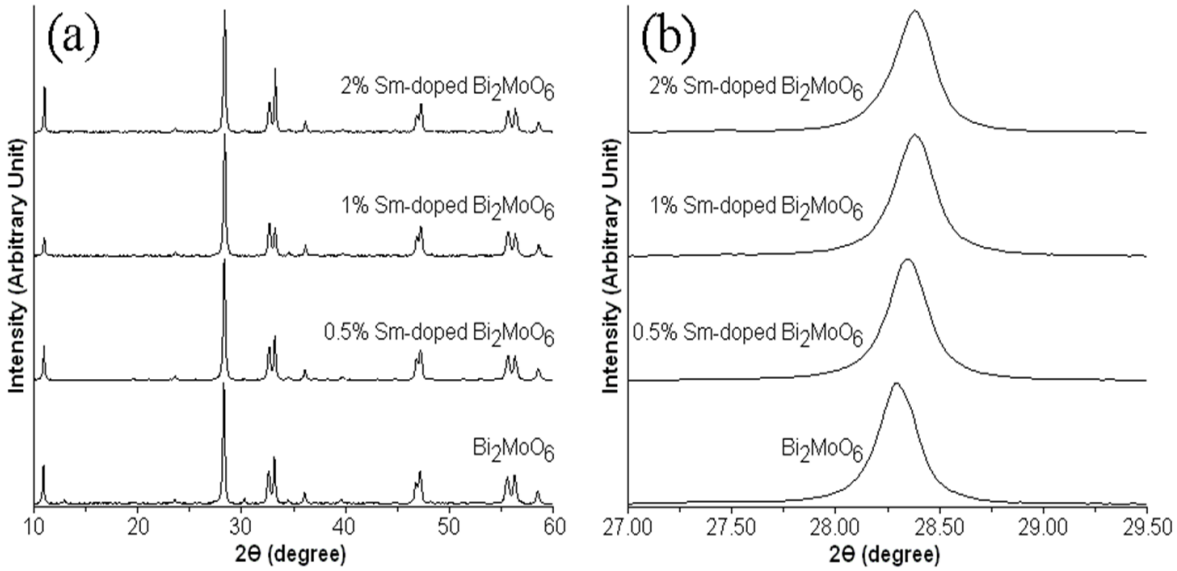

Figure 1. XRD patterns of 0–2% Sm-doped Bi_2MoO_6 samples at 2θ of (a) 10°–60° and (b) 27.00°–29.50°

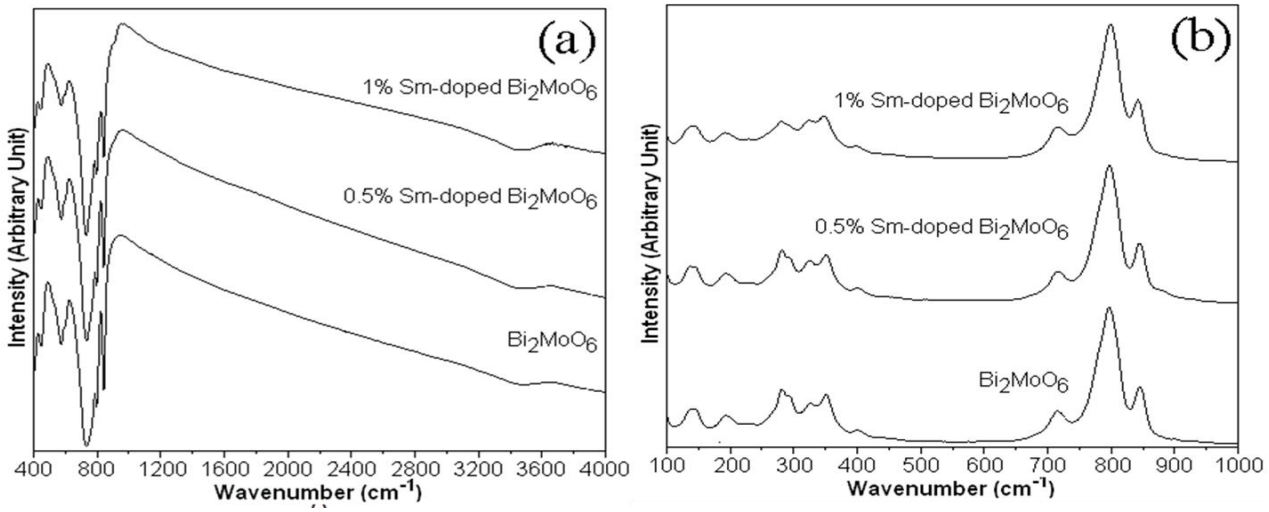

Figure 2. (a) FTIR and (b) Raman spectra of 0–1% Sm-doped Bi_2MoO_6 samples

Table 1. Unit cell, unit volume and particle size of Bi_2MoO_6 and Sm-doped Bi_2MoO_6 samples

Samples	Unit cell (Å)			Unit volume	Particle size
	a	b	c	($Å^3$)	(nm)
Bi_2MoO_6	5.4960	16.1707	5.4902	487.94	32.47
0.5% Sm-doped Bi_2MoO_6	5.4881	16.0793	5.4813	483.70	31.07
1% Sm-doped Bi_2MoO_6	5.4843	16.0615	5.4761	482.37	30.14
2% Sm-doped Bi_2MoO_6	5.4815	16.0259	5.4719	480.68	29.21

The asymmetric and symmetric stretching modes of the apical oxygen of Mo–O atoms in $[MoO_6]^{6-}$ octahedrons were detected at 842 and 796 cm^{-1} [1, 3, 4, 15, 16, 29]. The vibration of metal-oxygen of Sm-doped Bi_2MoO_6 was slightly shifted because of the change in the length and co-angular structure between $[Bi_2O_2]^{2+}$ layers and corner-shared octahedral structure of $[MoO_6]^{6-}$ [4, 16, 29, 30]. Fig. 2b is the Raman spectra of Bi_2MoO_6 and Sm-doped Bi_2MoO_6. Raman spectrum of Bi_2MoO_6 shows the main peaks at 715, 796 and 844 cm^{-1} which were assigned to the asymmetric stretching vibration (E_u mode) of Mo–O bond at equatorial oxygen atoms containing in the $[MoO_6]^{6-}$ octahedrons and symmetric and asymmetric stretching vibrations (A_{1g} and A_{2u} modes) of Mo–O bond at apical oxygen atoms of $[MoO_6]^{6-}$ octahedron [2, 16, 28, 33]. The minor Raman vibrations at 293 and 282 cm^{-1} correspond to the E_g bending vibration while the minor Raman vibration at 325, 351, and 399 cm^{-1} correspond to E_u symmetric bending [2, 16, 28, 33]. The Raman spectra of Sm-doped Bi_2MoO_6 became broaden due to the change in the metal-oxygen environment containing in Sm-doped Bi_2MoO_6 [16, 28, 33, 55].

10.57647/ijc.2026.1602.19

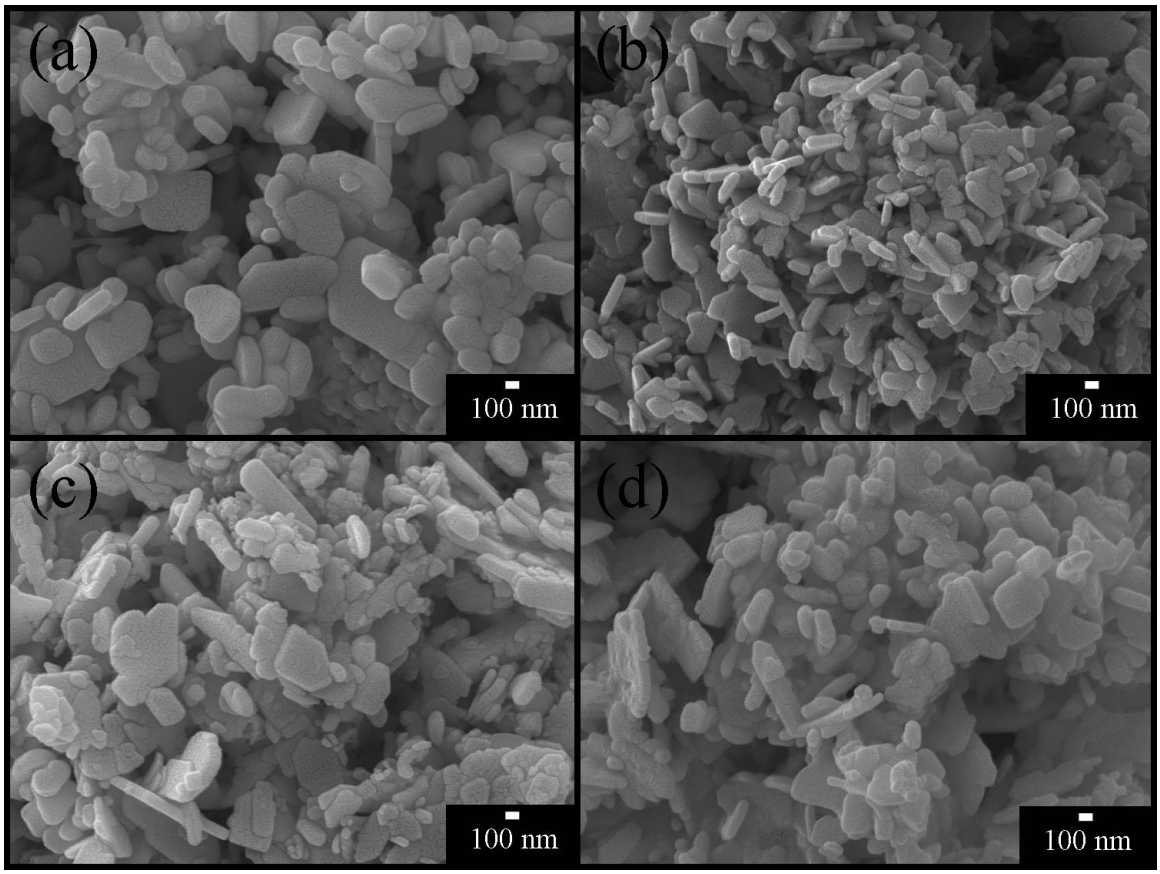

Figure 3. SEM images of (a) 0%, (b) 0.5%, (c) 1% and (d) 2% Sm-doped Bi_2MoO_6 samples

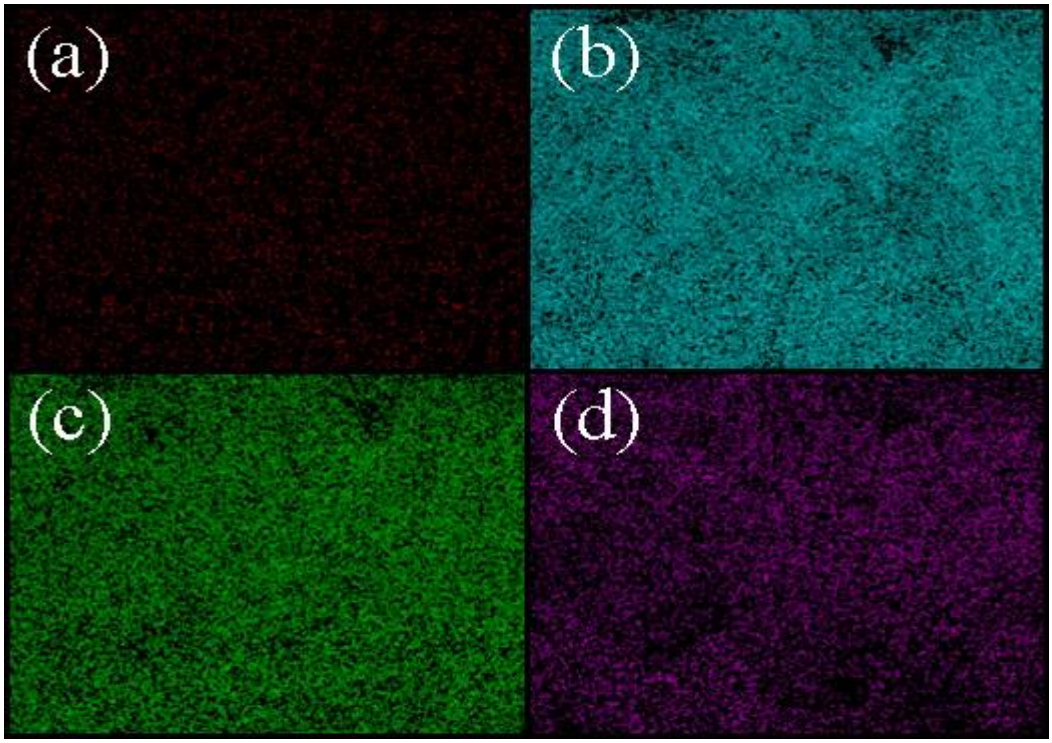

Figure 4. EDS maps of (a) Sm, (b) Bi, (c) Mo and (d) O elements containing in 2% Sm-doped Bi_2MoO_6 sample

Fig. 3 shows the SEM images of Bi_2MoO_6 and Sm-doped Bi_2MoO_6 prepared by hydrothermal method. The pure Bi_2MoO_6 sample was composed of uniform nanoplates with size of 300–800 nm. Bi_2MoO_6 nanoplates form a layered sandwich structure, specifically an Aurivillius-type structure, where perovskite-like $(MoO_2)^{2+}$ layers are intercalated between $(Bi_2O_2)^{2+}$ layers, creating distinct internal interfaces that contribute to the unique electronic and photocatalytic properties [3, 16, 30, 31, 40].

10.57647/ijc.2026.1602.19

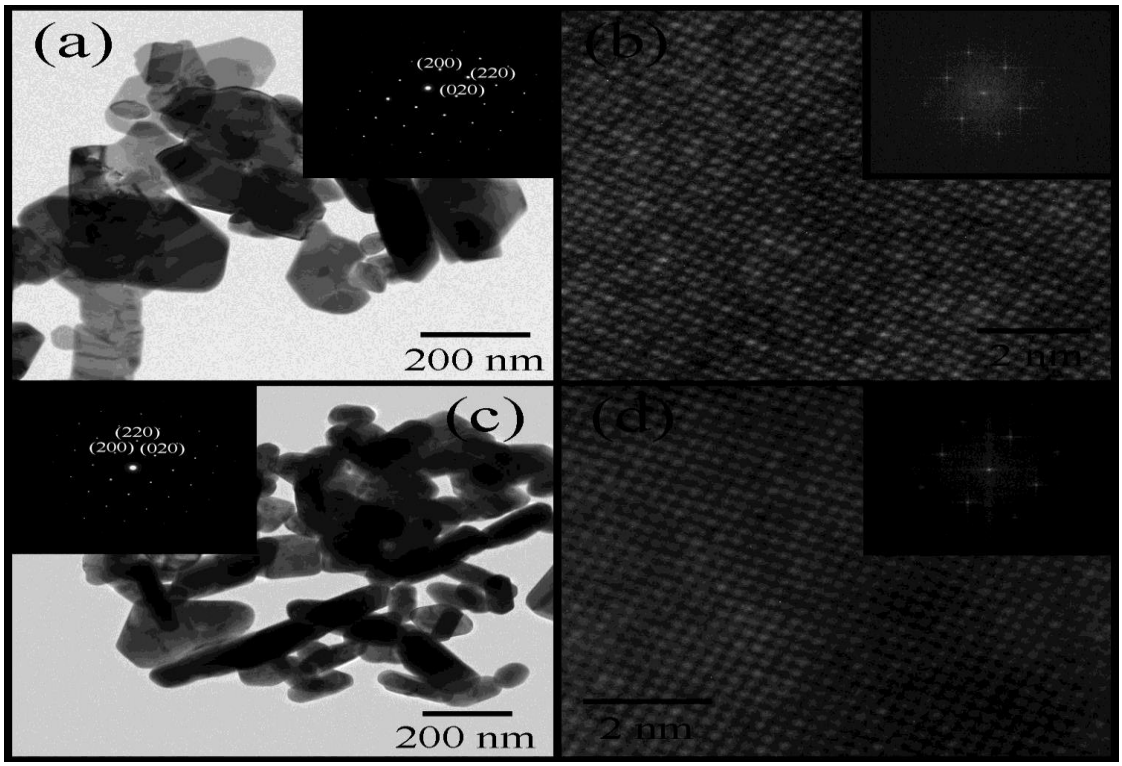

Figure 5. TEM images, SAED patterns, HRTEM images and FFT patterns of (a, b) Bi_2MoO_6 and (c, d) 1% Sm-doped Bi_2MoO_6

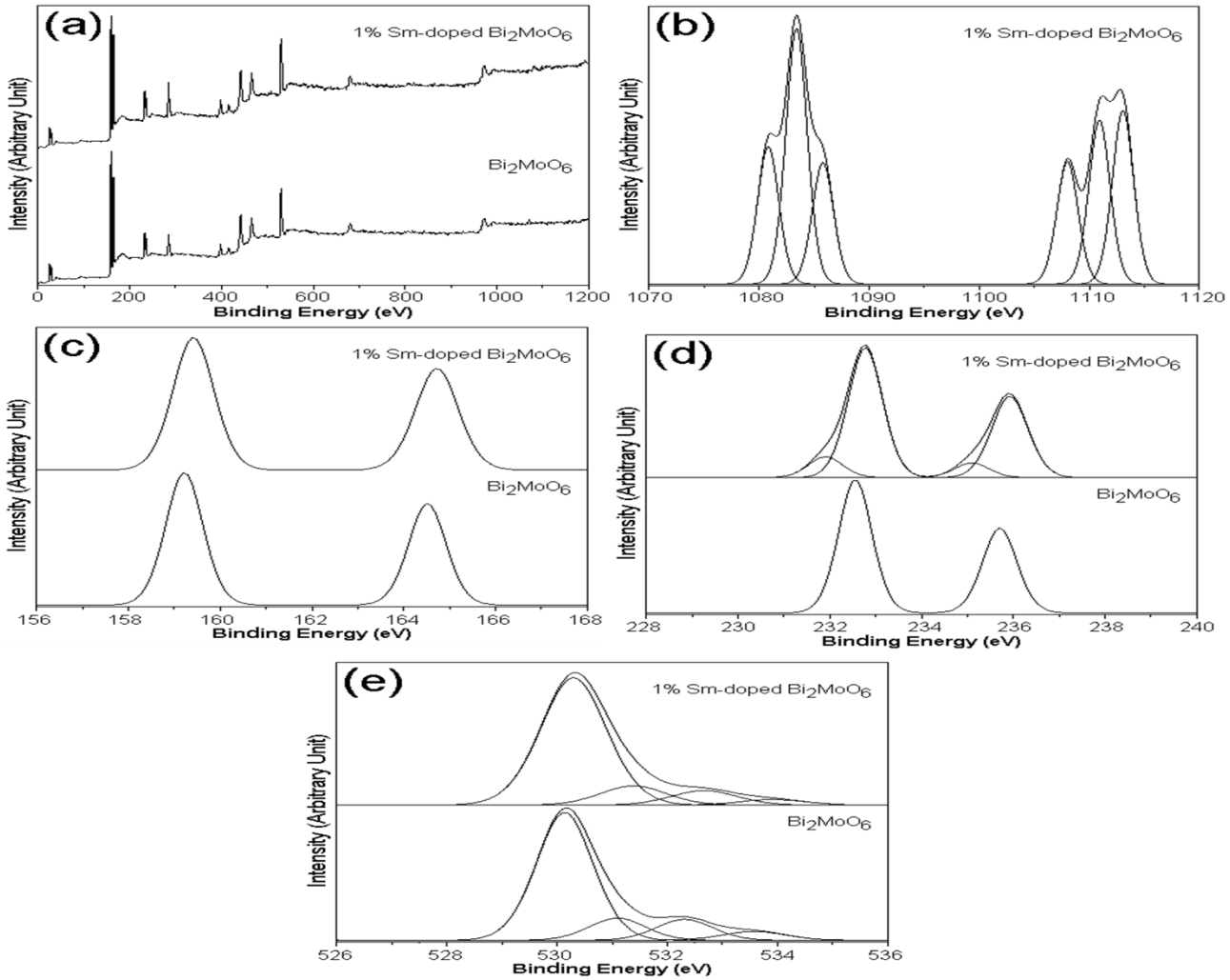

Figure 6. (a) Full survey scan XPS spectra of pure Bi_2MoO_6 and 1% Sm-doped Bi_2MoO_6. High resolution XPS spectra of (b) Sm 3d, (c) Bi 4f, (d) Mo 3d and (e) O 1s of pure Bi_2MoO_6 and 1% Sm-doped Bi_2MoO_6 samples

10.57647/ijc.2026.1602.19

Upon being loaded with Sm dopant, they show the uniform nanoplates with size of 200–400 nm. The size of Bi_2MoO_6 nanoplate became smaller because Sm^{2+} ions substituted for Bi^{3+} ions and the growth rate of Bi_2MoO_6 nanoplates was inhibited [16, 30-32]. The surface area of Bi_2MoO_6 nanoplates was increased and the pollutant adsorption was enhanced. In addition, visible light harvest on the nanoplate surface and the photocatalytic performance were improved [56, 57]. The distribution of individual element of Sm-doped Bi_2MoO_6 sample was analyzed by EDS (Fig. 4). The characteristic X-ray maps of Sm, Bi, Mo and O elements containing in 2% Sm-doped Bi_2MoO_6 appear as uniform distribution of elements containing in Bi_2MoO_6 lattice, including the existence of Sm ions across the Bi_2MoO_6 lattice.

Figs. 5a and 5c shows the TEM images of Bi_2MoO_6 and 1% Sm-doped Bi_2MoO_6 which present uniform nanoplates with size of ~200–300 nm for Bi_2MoO_6 and ~100–200 nm for 1% Sm-doped Bi_2MoO_6. The size and thickness of Bi_2MoO_6 nanoplates were slightly decreased by the loaded Sm dopant. The SAED patterns of individual Bi_2MoO_6 and 1% Sm-doped Bi_2MoO_6 nanoplates show the bright symmetric spots of electron diffraction of orthorhombic Bi_2MoO_6 single crystal. Both of them can be indexed to the (200), (220) and (020) planes of orthorhombic Bi_2MoO_6 structure (JCPDS no. 00-021-0102 [45]) with zone axis of [001].

The orthorhombic Bi_2MoO_6 nanoplate was composed of $(Bi_2O_2)^{2+}$ layers sandwiched between $(MoO_4)^{2-}$ layers along the b axis, leading to two-dimensional growth [29, 30, 38, 58]. HRTEM images of Bi_2MoO_6 and 1% Sm-doped Bi_2MoO_6 (Figs. 5b and 5d) present the crystallographic planes corresponding with orthorhombic Bi_2MoO_6 structure (JCPDS no. 00-021-0102 [45]). The Fast Fourier Transformation (FFT) image of Bi_2MoO_6 (inserted in Fig. 5b) reveals the periodic structure of orthorhombic Bi_2MoO_6 crystal and the symmetric electron diffraction of the single Bi_2MoO_6 crystal.

The surface compositions and chemical states of elements containing in Bi_2MoO_6 and 1% Sm-doped Bi_2MoO_6 were analyzed by XPS (Fig. 6) calibrated to the adventitious carbon C 1s peak centered at 285.1 eV. The full survey XPS spectra of Bi_2MoO_6 and 1% Sm-doped Bi_2MoO_6 reveal the presence of C, Bi, Mo and O for Bi_2MoO_6 and C, Sm, Bi, Mo and O for Sm-doped Bi_2MoO_6. The adventitious carbon C 1s peaks for both Bi_2MoO_6 and Sm-doped Bi_2MoO_6 were determined as a reference [3, 16, 59, 60].

Upon the use of Gaussian analysis, the high-resolution XPS spectrum of Sm 3d was fitted and corresponded to the binding energies at 1080.82, 1083.39 and 1085.78 eV for Sm $3d_{5/2}$ spin orbital and 1108.00, 1110.90 and 1113.04 eV for Sm $3d_{3/2}$ spin orbital [32, 61-65]. The binding energies at 1080.82 eV for Sm $3d_{5/2}$ and 1108.00 eV for Sm $3d_{3/2}$ correspond to the spin orbital of Sm^{2+} and those at 1083.39 eV for Sm $3d_{5/2}$ and 1110.90 eV for Sm $3d_{3/2}$ correspond to the spin orbital of Sm^{3+} [32, 61-63]. The binding energies at 1085.78 eV (Sm $3d_{5/2}$) and 1113.04 eV (Sm $3d_{3/2}$) are the strong charge-diffusion effect of 4f electrons and satellite of Sm^{3+} [63, 64].

The charge-diffusion of Sm^{3+} is influenced by the 4f electrons, shielded by the 5s and 5p electrons of the host lattice. The shielding effect can lead to reduce the role of the host lattice on charge-diffusion, allowing for more accurate prediction of the 4f and 5d energies of Sm^{3+}. The symmetric high resolution binding energies of Bi $4f_{7/2}$ and Bi $4f_{5/2}$ spin orbitals were detected at 159.22 and 164.52 eV for Bi_2MoO_6 and 159.41 and 164.72 eV for 1% Sm-doped Bi_2MoO_6, respectively. These belong to bismuth with tri-valence state [3, 16, 17, 22, 30, 32]. The symmetric high resolution binding energies at 232.54 eV of Mo $3d_{7/2}$ and 235.73 eV of Mo $3d_{5/2}$ for Bi_2MoO_6 and 232.80 eV of Mo $3d_{7/2}$ and 235.94 eV of Mo $3d_{5/2}$ for 1% Sm-doped Bi_2MoO_6 were identified as the existence of Mo^{6+} in both Bi_2MoO_6 and 1% Sm-doped Bi_2MoO_6 samples [3, 16, 17, 22, 30, 32].

Two minor energies at 231.93 eV (Mo $3d_{7/2}$) and 235.12 eV (Mo $3d_{5/2}$) for 1% Sm-doped Bi_2MoO_6 were assigned to the spin orbitals of Mo^{5+} [66, 67]. The asymmetric binding energies of O 1s spectra of Bi_2MoO_6 and 1% Sm-doped Bi_2MoO_6 were deconvoluted by Gaussian analysis. The peaks of binding energies at 530.14, 531.09, 532.32 and 533.59 eV of Bi_2MoO_6 and 530.30, 531.39, 532.68 and 533.91 eV of 1% Sm-doped Bi_2MoO_6 were attributed to the Bi–O bond, Mo–O bond and hydroxyl group on surfaces of the samples [3, 16, 17, 30, 32, 38].

The specific surface area and pore size distribution of Bi_2MoO_6 and 1% Sm-doped Bi_2MoO_6 samples were analyzed through the nitrogen adsorption-desorption isotherms (Fig. 7). The nitrogen adsorption-desorption isotherms of Bi_2MoO_6 and 1% Sm-doped Bi_2MoO_6 samples appear as hysteresis loops at P_0/P_t of 0.7–1.0 which can be categorized as type IV according to the IUPAC classification, and the Bi_2MoO_6 and 1% Sm-doped Bi_2MoO_6 samples were mesoporous [18, 19, 26, 27, 33, 34].

The specific surface area and average pore size calculated by Brunauer-Emmett-Teller (BET) and Barrett-Joyner-Halenda (BJH) formulae were 10.9045 $m^2.g^{-1}$ and 16.6058 nm for Bi_2MoO_6 and 11.4403 $m^2.g^{-1}$ and 13.3486 nm for 1% Sm-doped Bi_2MoO_6. Generally, introducing Sm dopant into Bi_2MoO_6 can lead to increase specific surface area and average pore size, create more active sites and pathways for pollutants, including promote charge separation and enhance photocatalytic efficiency of the photocatalyst [18, 19, 26, 27, 33, 34].

Fig. 8 shows the UV–visible absorption spectra of Bi_2MoO_6 and Sm doped-Bi_2MoO_6 recorded on the wavelength of 200–800 nm.

10.57647/ijc.2026.1602.19

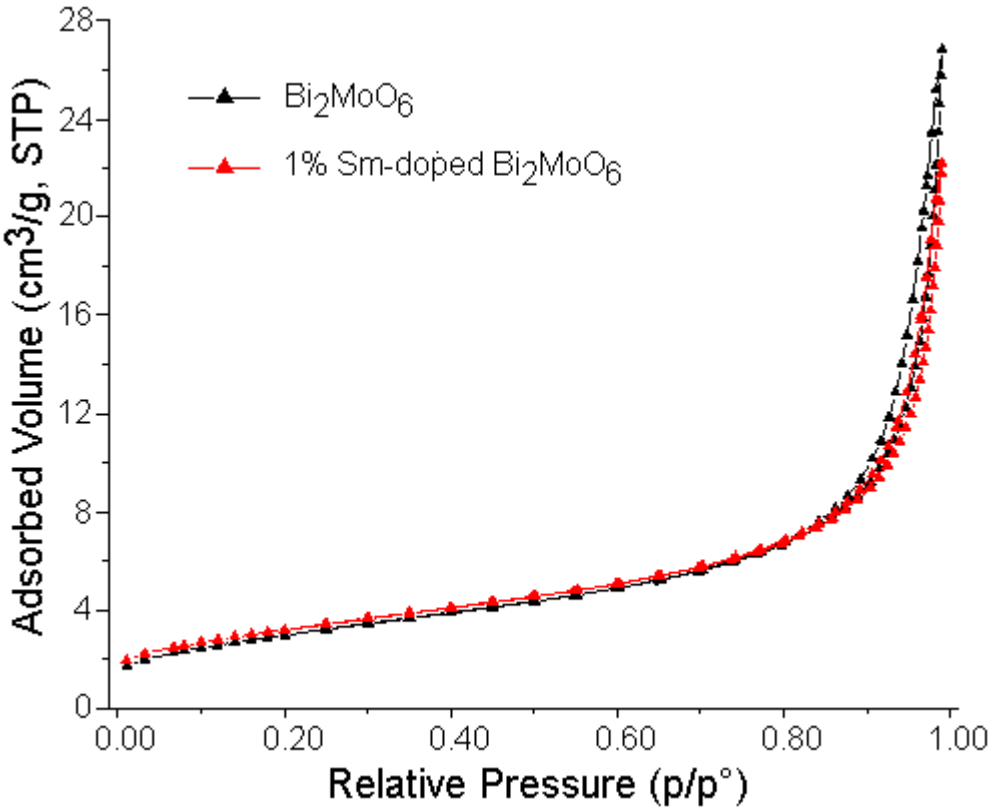

Figure 7. Nitrogen adsorption-desorption isotherms of Bi_2MoO_6 and 1% Sm-doped Bi_2MoO_6 samples

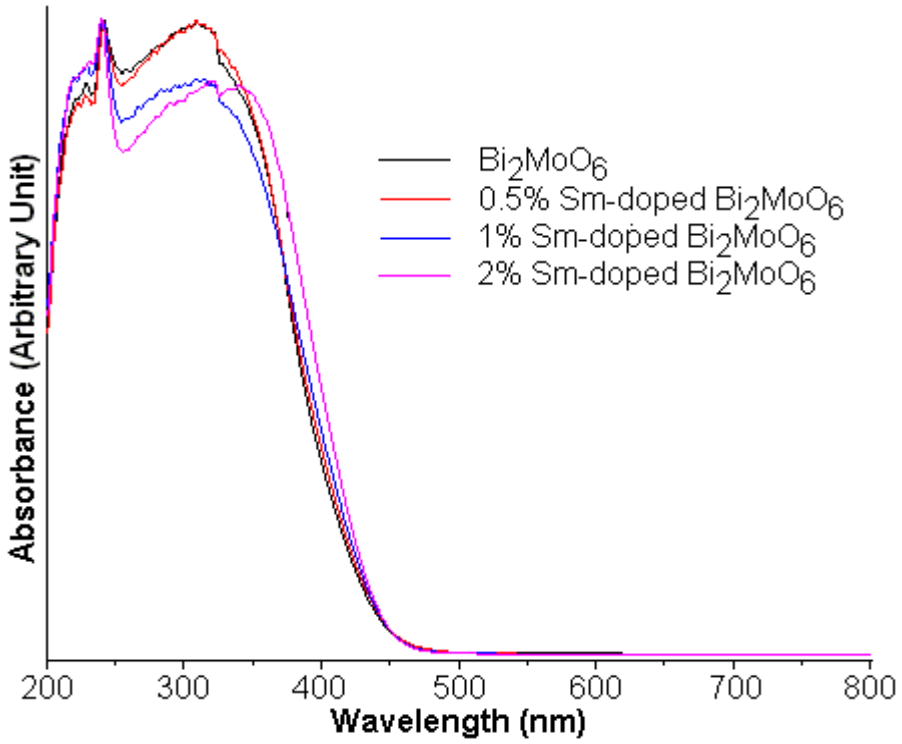

Figure 8. Absorption spectra of Bi_2MoO_6 and Sm-doped Bi_2MoO_6 samples

The spectrum of Bi_2MoO_6 shows the strong light absorption capacity from ultraviolet to visible range with the absorption edge of 441.53 nm because the Bi_2MoO_6 intrinsic band gap diffusion from VB to CB of O 2p orbitals were primarily from the Mo 4d orbitals of MoO_6 octahedrons and the absorption edge was believed to the secondary Bi 6p orbitals [2, 16, 68, 69]. Upon the introduction of Sm, the visible-light absorption range was obviously increased and the absorption edge was redshift from 441.53 nm of Bi_2MoO_6 to 443.23, 444.35 and 445.63 nm for 0.5%, 1% and 2% Sm-doped Bi_2MoO_6, respectively.

10.57647/ijc.2026.1602.19

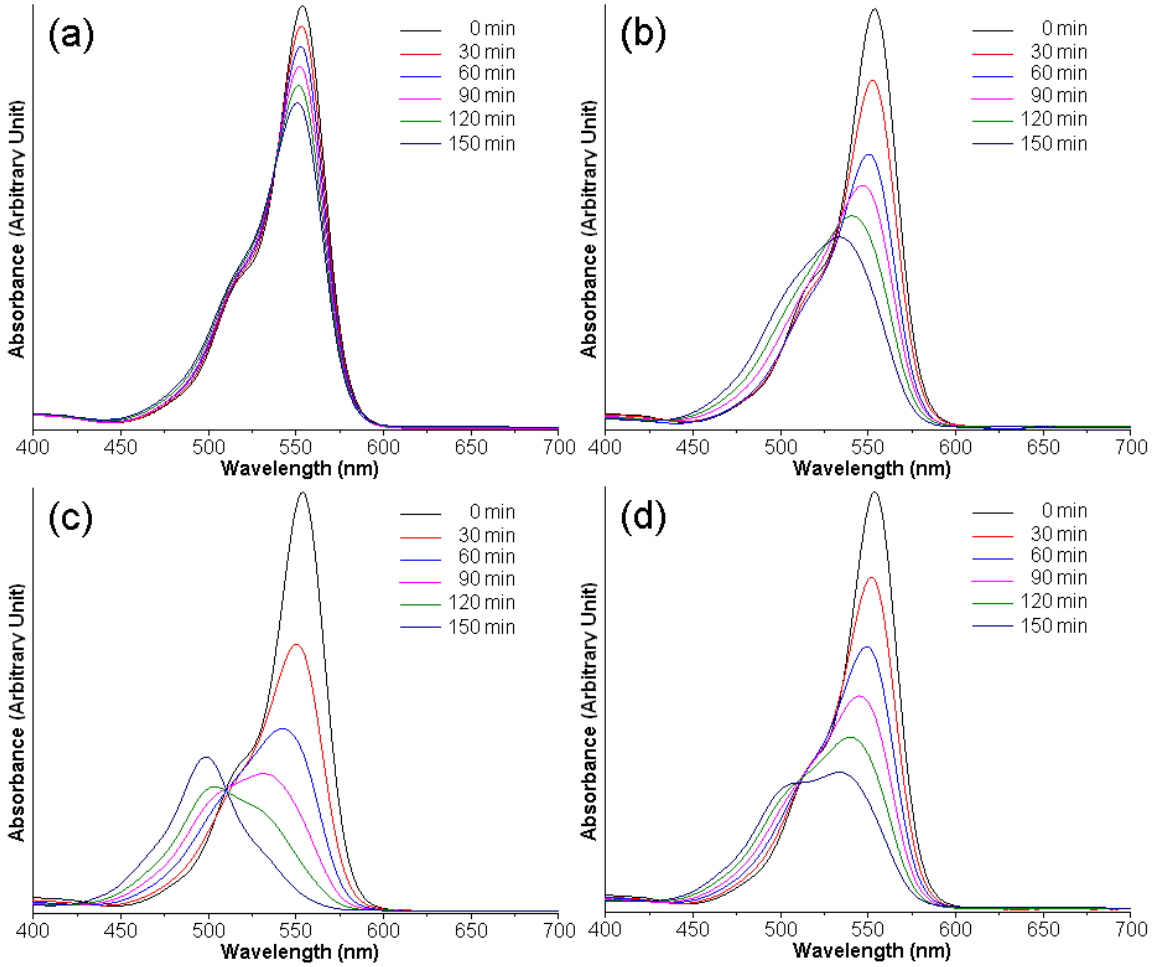

Figure 9. UV–visible absorption of RhB photocatalyzed by (a) 0%, (b) 0.5%, (c) 1% and (d) 2% Sm-doped Bi_2MoO_6 samples for different lengths of time

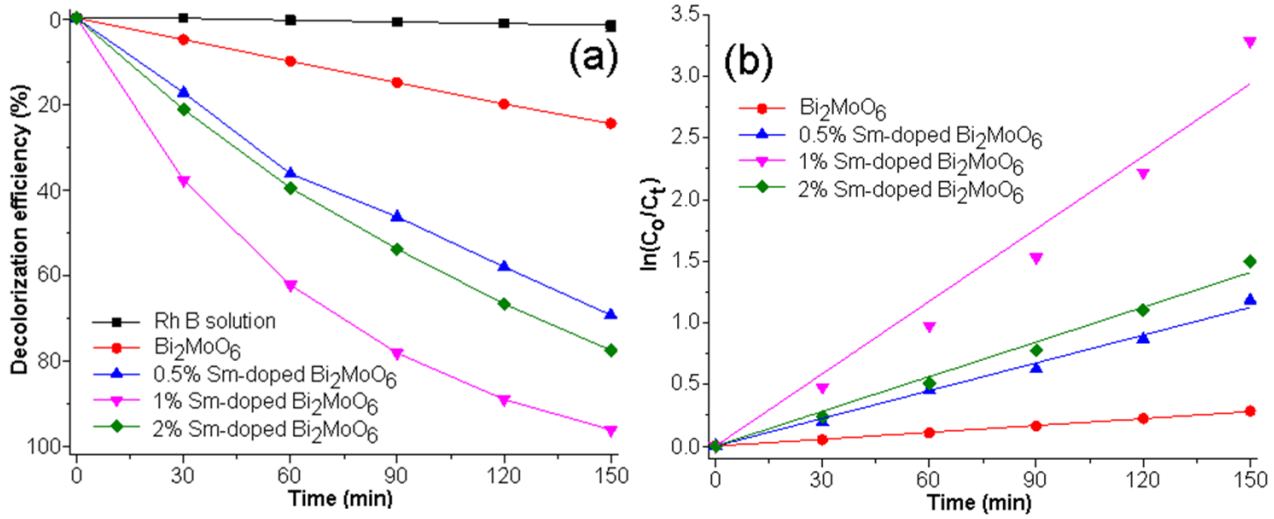

Figure 10. (a) Decolorization efficiencies and (b) linear plots for RhB degradation photocatalyzed by Bi_2MoO_6 and Sm-doped Bi_2MoO_6 samples compared with the blank test for different lengths of illumination time

Thus, the light absorption in visible range of Sm doped-Bi_2MoO_6 was able to absorb more photons during the photocatalytic reaction [31, 32, 70]. The band gap (E_g) of Bi_2MoO_6 and Sm doped-Bi_2MoO_6 was calculated as follows.

$$E_g = hc/\lambda \quad (2)$$

, where h, c and λ represent the Planck constant, speed of light and absorption edge wavelength, respectively [16, 41, 42, 71]. The band gap energies of as-prepared samples were 2.814, 2.803, 2.796 and 2.788 eV for 0%, 0.5%, 1% and 2% Sm-doped Bi_2MoO_6, respectively. The introduction of Sm played the role in narrowing the band gap of Bi_2MoO_6 by forming the impurity level in electronic band of Bi_2MoO_6 [16, 31, 32, 41].

10.57647/ijc.2026.1602.19

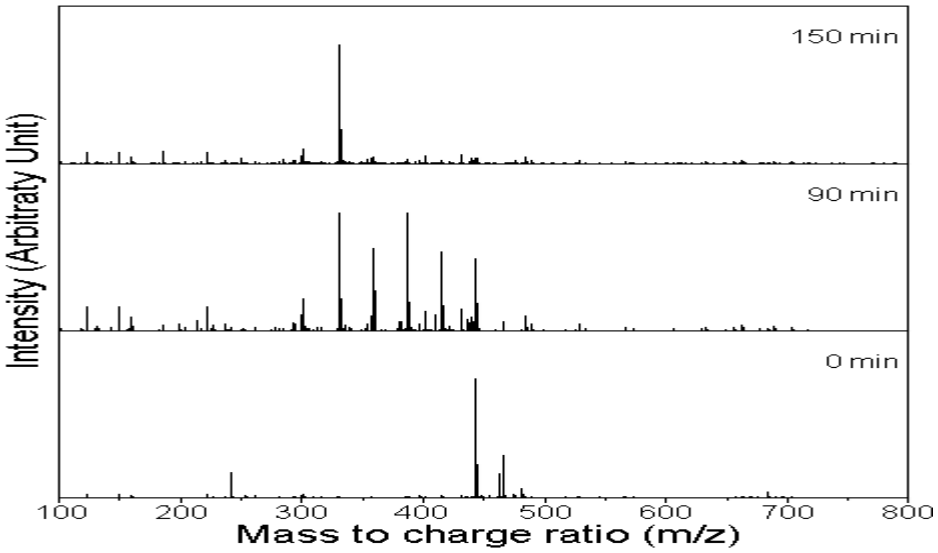

Figure 11. Mass spectra of RhB solutions photocatalyzed by 1% Sm-doped Bi_2MoO_6 sample for 0, 90 and 150 min

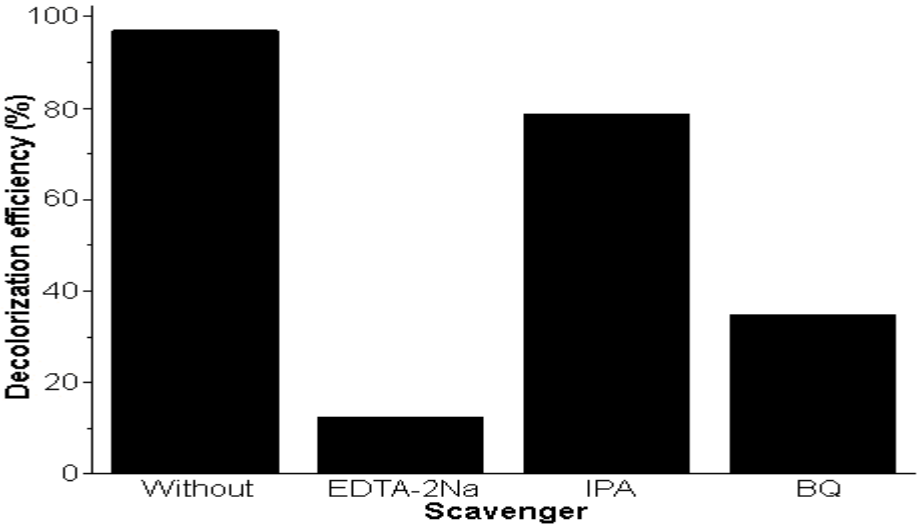

Figure 12. Decolorization efficiencies of 1% Sm-doped Bi_2MoO_6 sample for the degradation of RhB solutions with and without EDTA-2Na, IPA and BQ under visible light irradiation

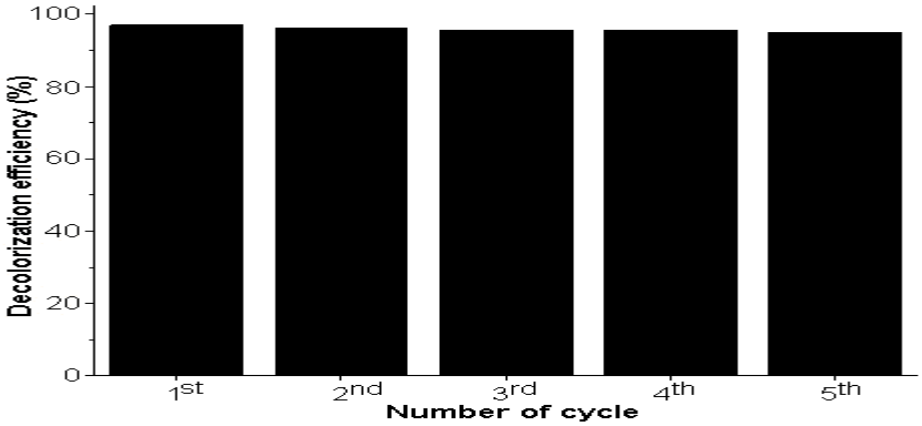

Figure 13. Stability and re-usability of 1% Sm-doped Bi_2MoO_6 photocatalyst for the gradation of RhB for five cycles

The photocatalytic performance of Bi_2MoO_6 containing different weight contents of Sm dopant was monitored through the RhB degradation under visible light irradiation. Fig. 9 shows the temporal UV-visible spectra of photodegraded RhB solutions photocatalyzed by Bi_2MoO_6 containing different weight contents of Sm dopant for different lengths of irradiation time. Clearly, the visible absorption peak of RhB at 554 nm for all the samples was monotonically decreased with the increase of irradiation time.

10.57647/ijc.2026.1602.19

Table 2. Comparison of photocatalytic efficiencies of the present and previous works

Photocatalysts	Organic compounds	Photocatalytic efficiencies	References
1.5 wt% g-C_3N_4/Bi_2MoO_6	MB	97% within 210 min	[18]
Sn-doped Bi_2MoO_6 nanosheets	Tetracycline (TC)	81.10% within 180 min	[23]
	2-mercaptobenzothiazole(MBT)	85.1% within 180 min	
1.5% Y doped Bi_2MoO_6	CR	85% within 180 min	[31]
8% Cd doped Bi_2MoO_6	Sulfamethoxazole (SMZ)	97.9% within 210 min	[33]
6% Gd/Bi_2MoO_6	RhB	84% within 100 min	[38]
Carbon-coated Bi_2MoO_6 composites	RhB	90% within 210 min	[73]
0.05% Er-doped Bi_2MoO_6	RhB	93.30% within180 min	[74]
C_3N_4/BiOBr/Bi_2MoO_6 composites	Ciprofloxacin (CIP)	94% within 240 min	[75]
	RhB	92% within 240 min	
5% Pt-doped Bi_2MoO_6 nanoparticles	RhB	80% within 180 min	[76]
9% Ag/Bi_2MoO_6 composites	RhB	77% within 120 min	[77]
3% Au-doped Bi_2MoO_6	RhB	96.25% within 240 min	[78]
MOF derived Bi_2MoO_6/TiO_2 nanohybrids	RhB	~92% within 180 min	[79]
1% Sm-doped Bi_2MoO_6	RhB	96.27% within 150 min	This work

The visible absorption peak of RhB by pure Bi_2MoO_6 was decreased less than that by Sm-doped Bi_2MoO_6 because the photo-excited electrons diffused from Bi_2MoO_6 to Sm^{3+} dopant as an electron acceptor and further combined with oxygen to form superoxide anion radical [41, 43, 44, 72]. At the end of 150 min, the peak position of RhB over 1% Sm-doped Bi_2MoO_6 was shifted to 498 nm by transforming the ethyl groups of RhB into rhodamine [3, 16, 25, 43].

The photocatalytic activities of Bi_2MoO_6 and Sm doped-Bi_2MoO_6 were evaluated through RhB degradation under visible light illumination. Fig. 10a shows the photocatalytic efficiency of Bi_2MoO_6 and Sm doped-Bi_2MoO_6 for RhB degradation under visible light illumination. The absorption intensity of pure RhB solution without the photocatalyst was remain unchanged under visible light irradiation. The pure RhB solution did not show any photolysis under visible light irradiation. The photocatalytic efficiency of Sm-doped Bi_2MoO_6 for RhB degradation was higher than that of pure Bi_2MoO_6 sample. When the loaded Sm was increased, the photocatalytic efficiency was also increased. The efficiency of 1% Sm-doped Bi_2MoO_6 was the highest of 96.27% or 3.91 times of Bi_2MoO_6 (24.65%) due to the increase of specific surface area and visible light harvest [18, 19, 31, 33, 34, 41]. Upon further increase the loaded Sm to 2% Sm dopant, the efficiency of 2% Sm-doped Bi_2MoO_6 became weaker because Sm dopant was excessive [32, 41, 43].

Comparting to the previous reports (Table 2), 1% Sm-doped Bi_2MoO_6 nanoplates have the highest photocatalytic performance [18, 23, 31, 33, 38, 73-79]. The Sm dopant is a promising candidate in improving the photocatalytic performance of the semiconductor. The kinetic photocatalytic constant of Bi_2MoO_6 and Sm-doped Bi_2MoO_6 for RhB degradation under visible light illumination was calculated by the Langmuir-Hinshelwood model as follows.

$$\ln(C_o/C_t) = kt \quad (3)$$

C_o and C_t are the content of RhB before and after visible light illumination at a certain time (t) and k is the apparent kinetic constant [3, 15, 16, 29, 43, 80]. Fig. 10b shows the linear relationship between $\ln(C_o/C_t)$ versus visible light illumination time (t) with correlation coefficient (R^2) → 1. The reaction followed the pseudo-first-order model [1, 3, 16, 29]. The calculated kinetic constants were $1.85x10^{-3}$, $7.53x10^{-3}$, 0.0196 and $9.38x10^{-3}$ min^{-1} for 0%, 0.5%, 1% and 2% Sm-doped Bi_2MoO_6, respectively. The 1% Sm-doped Bi_2MoO_6 sample has the highest kinetic photocatalytic constant for RhB degradation under visible light illumination. This certifies that Sm dopant acted as an electron accepter which played the role in narrowing band gap and suppressing the recombination of photo-induced charge carriers during photocatalytic reaction [31, 33, 34, 41, 44].

The degradation pathway of RhB photocatalyzed by 1% Sm-doped Bi_2MoO_6 was investigated by mass spectroscopy (Fig. 11). Mass spectrum of RhB solution stirred in the dark condition for 30 min presents the mass-to-charge ratio (m/z) of 443 for a positive electrospray ionization (ESI^+) mode [81, 82]. Upon being photocatalyzed for 90 min, the intensity of m/z at 443 was reduced. They indicate that the positively charged RhB+ molecules were degraded by active species such as hydroxyl radical ($^{\bullet}OH$), superoxide anion ($^{\bullet}O_2^-$) and hole (h^+). New m/z ratios at 415, 387, 359 and 311 corresponded to the N,N,N′-triethyl-rhodamine (m/z = 415), N,N′-diethyl-rhodamine (m/z = 387), N-ethyl-rhodamine (m/z = 359) and rhodamine (m/z = 311).

10.57647/ijc.2026.1602.19

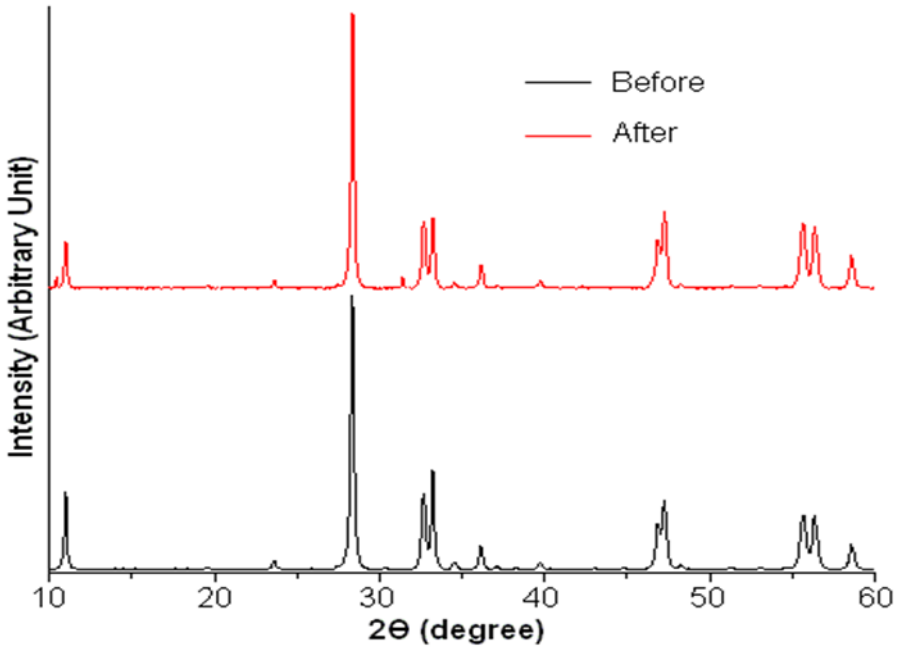

Figure 14. Comparison of XRD patterns of the fresh and five-cycle test of re-used 1% Sm-doped Bi_2MoO_6 nanoplates

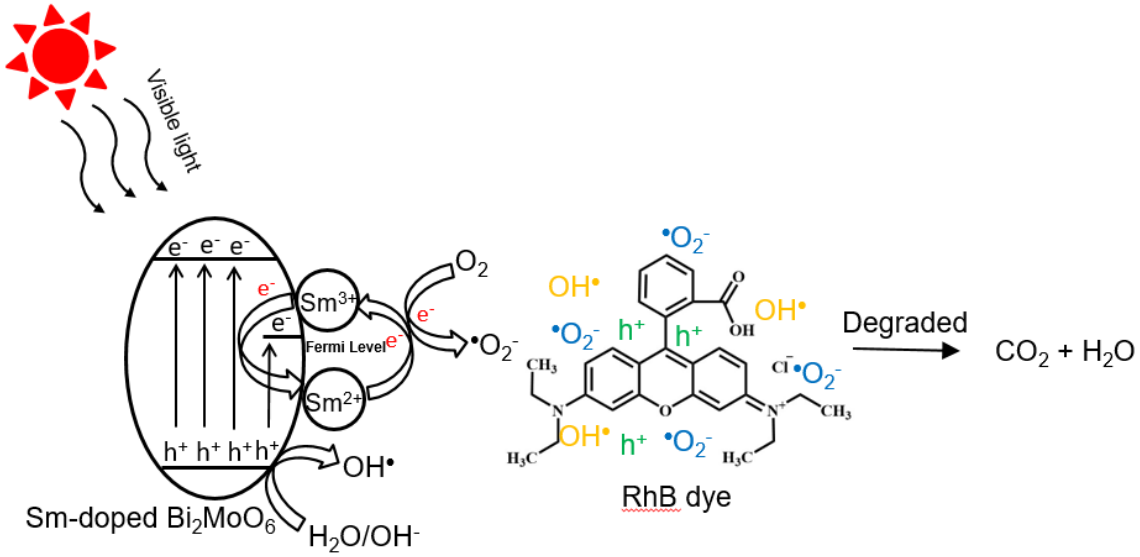

Figure 15. A proposed photocatalytic mechanism of Sm-doped Bi_2MoO_6 for RhB degradation illuminated by visible radiation

The results show that the positively charged RhB^+ molecules were degraded the full ethyl group by N-deethylation pathway [81, 83-85]. Subsequently, rhodamine molecules (m/z = 311) were cleaved through the chromophore pathway. Thus, several aromatic intermediates with m/z of 301, 294, 221, 185 and 149 were produced and further converted into H_2O, CO_2 and inorganic ions as final products through the mineralization process [81, 83-85].

Active radicals for RhB degradation photocatalyzed by 1% Sm-doped Bi_2MoO_6 illuminated by visible light were investigated using isopropanol (IPA), benzoquinone (BQ) and ethylenediaminetetraacetic acid disodium salt (EDTA- 2Na) for trapping $^{\bullet}OH$, $^{\bullet}O_2^-$ and h^+, respectively [16, 32, 86-88]. Fig. 12 shows the trapping test of photocatalytic efficiency for RhB degradation photocatalyzed by 1% Sm-doped Bi_2MoO_6 under visible light irradiation. The photocatalytic efficiencies were significantly inhibited to 34.68% and 12.35% by the use of BQ and EDTA-2Na, respectively. They identified that $^{\bullet}O_2^-$ and h^+ are the main active species for RhB degradation [16, 32, 86, 87]. The photocatalytic efficiency was little decreased by IPA adding, therefore, $^{\bullet}OH$ has a little effect on the RhB degradation photocatalyzed by 1% Sm-doped Bi_2MoO_6 under visible light irradiation [16, 32, 86, 87].

Fig. 13 shows the recycled experiment to study the durability and stability of the 1% Sm-doped Bi_2MoO_6 photocatalyst for RhB degradation under visible light irradiation. The stability and durability of reused 1% Sm-doped Bi_2MoO_6 nanoplates were very excellent even at the end of cycle five. The XRD pattern of the reused 1%

10.57647/ijc.2026.1602.19

Sm-doped Bi_2MoO_6 nanoplates at the end of cycle five was compared with the XRD pattern of the fresh 1% Sm-doped Bi_2MoO_6 nanoplates. According to Fig. 14, the structure of the reused 1% Sm-doped Bi_2MoO_6 nanoplates can be indexed to the orthorhombic Bi_2MoO_6 structure (JCPDS no. 00-021-0102 [45]). Clearly, the 1% Sm-doped Bi_2MoO_6 nanoplates are significantly stable and extremely good in photocatalytic performance.

Fig. 15 shows the photocatalytic mechanism of Sm-doped Bi_2MoO_6 nanoplates for the photodegradation of RhB under visible light irradiation. The mechanism is explained by the following.

$$\text{Sm-doped } Bi_2MoO_6 + hv \rightarrow e^-_{CB(Bi2MoO6)} + e^-_{Fermi\ Level} + h^+_{VB(Bi2MoO6)} \quad (4)$$

$$e^-_{Fermi\ Level} + Sm^{3+} \rightarrow Sm^{2+} \quad (5)$$

$$Sm^{2+} + O_2 \rightarrow {}^{\bullet}O_2^- + Sm^{3+} \quad (6)$$

$$h^+_{VB(Bi2MoO6)} + H_2O/OH^- \rightarrow OH^{\bullet} \quad (7)$$

$$RhB + {}^{\bullet}O_2^-/OH^{\bullet} \rightarrow CO_2 + H_2O + \text{inorganic ions} \quad (8)$$

Sm-doped Bi_2MoO_6 nanoplates were excited by visible light. Some electrons were in conduction band (CB) and some were in Fermi level. The excited electrons diffused from Fermi level to Sm^{3+} with the reaction of Sm^{2+} and O_2 to produce ${}^{\bullet}O_2^-$. Concurrently, photo-induced holes in valence band (VB) combined with adsorbed H_2O/OH^- to produce $OH^{\bullet}$ [16, 32, 43, 89, 90, 91]. According to the previous report, Jiang et al. found that the photocatalytic activity of $BiVO_4$ was improved by the loaded Sm dopant because Sm^{3+} ions played the role in accepting the photo-electrons which further reacted with adsorbed O_2 to form ${}^{\bullet}O_2^-$ radicals [44]. Thus, the recombination of charge-carriers containing in Bi_2MoO_6 was restrained and the separation of charge-carriers was enhanced. In addition, lifetime of the separated charge-carriers was prolonged and the photocatalytic performance of Sm-doped Bi_2MoO_6 was improved [16, 17, 32, 43, 89, 90]. O_2 and H_2O/OH^- reacted with the photo-electrons and photo-induced holes to form ${}^{\bullet}O_2^-$ and $OH^{\bullet}$ radicals, respectively. In the end, RhB molecules were degraded by the active radicals and were transformed into CO_2 and H_2O as final products [16, 17, 32, 43, 89].

4. Conclusions

In summary, Sm-doped Bi_2MoO_6 nanoplates as visible-light-driven photocatalyst were successfully synthesized by hydrothermal method. The analytical results showed that orthorhombic Sm-doped Bi_2MoO_6 nanoplates played the role in harvesting visible-light range better than pure Bi_2MoO_6 nanoplates. The 1% Sm doped-Bi_2MoO_6 nanoplates with excellent stability and re-usability have the highest photocatalytic activity for degradation of RhB by ${}^{\bullet}O_2^-$ and h^+ as the main active species. Thus, they are the promising visible-light-driven photocatalyst used for wastewater treatment.

Acknowledgments

This work was supported by Prince of Songkla University (Ref. No. SCI6801375S), Thailand Science Research and Innovation (TSRI) [Grant number FRB690047/0230], and National Science, Research and Innovation Fund (NSRF).

Funding Declaration
No funding was received from any governmental or non-governmental organization to conduct this research.

Data availability
All the data generated or obtained from analyses of this study are included in the article and its supplementary information file.

Supplementary information
Not Applicant (N. A.)

References

[1] T. Chankhanittha, V. Somaudon, J. Watcharakitti, V. Piyavarakorn, and S. Nanan. *Mater. Lett.*, **258**(2020):126764. https://doi.org/10.1016/j.matlet.2019.126764

[2] J. Xue, F. Li, S. Li, J. Zhang, and Q. Bi. *Int. J. Electrochem. Sci.*, **17**(2022):220136. https://doi.org/10.20964/2022.01.29

[3] Phuruangrat, P. Keereesaensuk, K. Karthik, P. Dumrongrojthanath, N. Ekthammathat, S. Thongtem, and T. Thongtem. *J. Inorg. Organomet. Polym. Mater.*, **30**(2020):322–329. https://doi.org/10.1007/s10904-019-01190-4

[4] J. Wang, Y. Sun, Z. Wang, C. Wu, and P. Rao. *Russ. J. Phys. Chem. A*, **93**(2019):736–742. https://doi.org/10.1134/S0036024419040307

[5] J. Du, I. Ahmad, I.M. Ashraf, F.B.M. Ahmed, A. Aslam, I. Ali, A. Mohammad, and M.A. Khasawneh. *Inter. J. Hydro. Energy*, **100**(2025):1361-1384. https://doi.org/10.1016/j.ijhydene.2024.12.421

[6] Ahmad, R. Bousbih, A. Mahal, W.Q. Khan, M. Aljohani, M.A. Amin, N.N.A. Jafar, M.S. Jabir, H. Majdi, A.S. Alshomrany, M. Shaban, I. Ali, and H. Bayahia. *Mater. Sci. Semicond. Process.*, **180**(2024):108578.

[7] H. Lee, S.H. Park, Y.K. Park, B.H. Kim, S.J. Kim, and S.C. Jung. Chem. Cent. J., **7**(2013):156. https://doi.org/10.1186/1752-153X-7-156

[8] S. Singh, N. Parveen and H. Gupta. *Environ. Technol. Innov.*, **12**(2018):189-195. https://doi.org/10.1016/j.eti.2018.09.001

[9] G. Muthuraman, and T.T. Teng. *J. Indust. Eng. Chem.*, **15**(2009):841-846. https://doi.org/10.1016/j.jiec.2009.09.010

[10] S.S. Imam, and H.F. Babamale. *Asian J. Chem. Sci.*, **7**(2020):25-37. https://doi.org/10.9734/AJOCS/2020/v7i119013

[11] H. Li, W. Li, F. Wang, X. Liu, C. Ren, and X. Miao. *Appl. Surf. Sci.*, **427**(2018):1046-1053. http://dx.doi.org/10.1016/j.apsusc.2017.09.106

[12] Ahmad, S. Shukrullah, M.Y. Naz, E. Ahmed, M. Ahmad, A.J. Obaidullah, A. Alkhouri, A. Mahal, and Y.Y. Ghadi. *Mater. Sci. Semicond. Process.*, **172**(2024):108088. https://doi.org/10.1016/j.mssp.2023.10808

[13] L. Sawunyama, O.A. Oyewo, S.S. Makgato, M.F. Bopape, and D.C. Onwudiwe. *Discover Nano*, **20**(2025):1. https://doi.org/10.1186/s11671-024-04178-3

[14] Y. Liu, F. Zhou, S. Zhan, and Y. Yang. *J. Inorg. Organomet. Polym. Mater.*, **27**(2017):1365–1375. https://doi.org/10.1007/s10904-017-0590-0

[15] Y. Liu, F. Zhou, S. Zhan, Y. Yang, and Y. Yin. *Chem. Res. Chin. Univ.*, **32**(2016):284-290. https://doi.org/10.1007/s40242-016-5315-3

[16] Phuruangrat, S. Buapoon, T. Bunluesak, P. Suebsom, S. Thongtem, and T. Thongtem. *J. Aust. Ceram. Soc.*, **58**(2022):71–82. https://doi.org/10.1007/s41779-021-00665-3

[17] V. Shanmugam, A.L. Muppudathi, S. Jayavel, and K.S. Jeyaperumal. *Arabian J. Chem.*, **13**(2020):2439–2455. https://doi.org/10.1016/j.arabjc.2018.05.009

[18] Z. Qin, C. Liu, J. Tan, H. Mei, W. Xue, and W. Wei. *Res. Chem. Intermed.*, **51**(2025):1491–1510. https://doi.org/10.1007/s11164-025-05503-w

[19] H. Pan, N. Xu, Y. Zhang, L. Liu, J. He, and H. Xie. *J. Mater. Res.*, **40**(2025):463–476. https://doi.org/10.1557/s43578-024-01510-6

[20] Y. Chen, X. Su, C. Yang, L. Dou, J. Zhong, and M. Li. *Mater. Chem. Phys.*, **326**(2024):129860. https://doi.org/10.1016/j.matchemphys.2024.129860

[21] M. Chakraborty, S. Ghosh, and V. Mahalingam. *Energy Fuels*, **4**(2020):1507-1514. https://doi.org/10.1039/C9SE00796B

[22] J. Zhao, Y. Yang, W. Yu, Q. Ma, X. Dong, X. Wang, J. Wang, and G. Liu. *J. Mater. Sci.: Mater. Electron.*, **28**(2017):543–552. https://doi.org/10.1007/s10854-016-5557-3

[23] S. Cao, L. Li, J. Dong, B. Wang, H. Wei, M. Ji, G. Liu, J. Xia, and H. Li. *J. Alloy. Compds.*, **1010**(2025):177807. https://doi.org/10.1016/j.jallcom.2024.177807

[24] G. Ren, S. Liu, Z. Li, H. Bai, X. Hu, and X. Meng. *Sol. RLL*, **6**(2022):2200154. https://doi.org/10.1002/solr.202200154

[25] L. Xie, J. Ma, and G. Xu. Mater. Chem. Phys., **110**(2008):197–200. https://doi.org/10.1016/j.matchemphys.2008.01.035

[26] A.M. Cruz, and S.O. Alfaro. *J. Mole. Catal. A*, **320**(2010):85–91. https://doi.org/10.1016/j.molcata.2010.01.008

[27] Q. Wang, J. Ge, W. Liu, H. Zhang, and R. Li. *Catalysts*, **15**(2025):198. https://doi.org/10.3390/catal15030198

[28] Y. Miao, G. Pan, Y. Huo, and H. Li. *Dyes Pigm.*, **99**(2013):382-389. http://dx.doi.org/10.1016/j.dyepig.2013.05.005

[29] Phuruangrat, P. Dumrongrojthanath, B. Kuntalue, S. Thongtem, and T. Thontem. *Mater. Lett.*, **196**(2017):256-259. https://doi.org/10.1016/j.matlet.2017.03.073

[30] Z. Liu, X. Liu, C. Yu, L. Wei, and H. Ji. *Sep. Purif. Technol.*, **247**(2020):116951. https://doi.org/10.1016/j.seppur.2020.116951

[31] H. Qiu, S. Liu, X. Ma, Y. Li, Y. Fan, W. Li, and H. Zhou. *J. Miner. Metall. Mater.*, **30**(2023):1824 https://doi.org/10.1007/s12613-023-2656-z

[32] M. Wang, M. You, P. Guo, H. Tang, C. Lv, Y. Zhang, T. Zhu, and J. Han. *J. Alloy. Compds.*, **728**(2017):739-746. https://doi.org/10.1016/j.jallcom.2017.09.066

[33] B. Zhang, C. Fang, J. Ning, R. Dai, Y. Liu, Q. Wu, F. Zhang, W. Zhang, S. Dou, and X. Liu. *Carbon Neutraliz.*, **2**(2023):646–660. https://doi.org/10.1002/cnl2.96

[34] L. Yan, J. Tang, Q. Qiao, H. Cai, Y. Dong, J. Jin, Y. Xu, and H. Gao. *Nanomaterials*, **13**(2023):214. https://doi.org/10.3390/nano13010214

[35] C.N. Ri, S.G. Kim, K.S. Ju, H.S. Ryo, C.H. Muna, and U.H. Kim. *RSC Adv.*, **8**(2018):5433–5440. https://doi.org/10.1039/c7ra12766a

[36] Y. Ma, Y. Jia, Y. Lin, and W. Shi. *Dalton Trans.*, **48**(2019)12009-12012. https://doi.org/10.1039/C9DT02028D

[37] D. Wang, H. Shen, L. Guo, C. Wang, F. Fu, and Y. Liang. *Appl. Surf. Sci.*, **436**(2018):536–547. https://doi.org/10.1016/j.apsusc.2017.12.002

[38] H. Li, X. Yu, X. Hao, Z. Zhang, Y. Wang, and J. Li. *Nanomaterials*, **10**(2020):646. https://doi.org/10.3390/nano10040646

[39] X. Yang, X. Li, B. Zhang, T. Liu, and Z. Chen. *ACS Sustainable Chem.* Eng., **12**(2024):6519−6528. https://doi.org/10.1021/acssuschemeng.3c07871

[40] Q. Sun, M. Ke, Y. Zhao, B. Wang, J. Zhang, and J. Sheng. *Appl. Surf. Sci.*, **563**(2021):150104. https://doi.org/10.1016/j.apsusc.2021.150104

[41] C. Yu, Z. Wu, R. Liu, H. He, W.g Fan, and S. Xue. *J. Phys. Chem. Solids*, **93**(2016):7–13. http://dx.doi.org/10.1016/j.jpcs.2016.02.008

[42] Y. Chen, L. Wang, J. Zhong, M. Li, H. Fan, and C. Tian. *Desalin. Water Treat.*, **235**(2021):200–208. https://doi.org/10.5004/dwt.2021.27586

[43] X. Zhang, M. Zhang, and K. Cao. CrystEngComm, **21**(2019):6208-6218. https://doi.org/10.1039/C9CE01043B

[44] C.Z. Jiang, X.D. Lu, Y.Q. Tan, and S. Bai. *Adv. Mate. Res.*, **391-392**(2012):1283-1286. http://dx.doi.org/10.4028/www.scientific.net/AMR.391-392.1283

[45] Powder Diffract. File, JCPDS-ICDD, 12 Campus Blvd., Newtown Square, PA 19073-3273, U.S.A., (2004).

[46] S.S. Priya, and V.A. Ferby. *Ceram. Inter.*, **50**(2024):40729-40735. https://doi.org/10.1016/j.ceramint.2024.07.114

[47] T.A. Jose, T. Krishnapriya, A. Jose, C.S. Rajesh, C. Joseph, and P.R. Biju. *J. Alloy. Compds.*, **963**(2023):171104. https://doi.org/10.1016/j.jallcom.2023.171104

[48] S. Yuan, Y. Zheng, Y. Chu, C. Xia, R. Dong, J. Xu, B. Teng, Y. Wu, and Y. He. *Green Energy Environ.*, (2025) In Press. https://doi.org/10.1016/j.gee.2025.07.005

[49] S. Patil, S. Seal, Y. Guo, A. Schulte, and J. Norwood. *Appl. Phys. Lett.*, **88**(2006):243110. https://doi.org/10.1063/1.2210795

[50] S. Kobayashi, Y. Ikuhara, and T. Mizoguchi. *Phys. Rev. B*, **98**(2018):134114. https://doi.org/10.1103/PhysRevB.98.134114

[51] V.A. Gushchina, A.G. Son, A.A. Egorova, A.A. Arkhipenko, M.A. Teplonogova, N.N. Efimov, and S.A. Kozyukhin. *Russ. J. Inorg. Chem.*, **69**(2024):940–948. https://doi.org/10.1134/S0036023624600928

[52] Phuruangrat, Y. Chimupala, A. Somdee, T. Thongtem, and S. Thongtem. *Russ. J. Phys. Chem. A*, **99**(2025):808–820. https://doi.org/10.1134/S003602442570041

[53] Z. Qiang, X. Liu, F. Li, T. Li, M.g Zhang, H. Singh, M. Huttul, and W. Cao. *Chem. Eng. J.*, **403**(2021):126327. https://doi.org/10.1016/j.cej.2020.126327

[54] J. He, W. Wang, F. Long, Z. Zou, Z. Fu, and Z. Xu. *Mater. Sci. Eng. B*, **177**(2012):967-974. https://doi.org/10.1016/j.mseb.2012.04.018

[55] I.M. Pinatti, F.A. Pires, P.B. Almeida, P.F.S. Pereira, M.D. Teodoro, E. Guillamón, A.Z. Simões, J. Andrés, E. Longo, and I.L.V. Rosa. *J. Lumin.*, **243**(2022):118675. https://doi.org/10.1016/j.jlumin.2021.118675

[56] O.A. Oyewo, W.R. Abd-Ellatif, S.S. Makgato, H.M. Sabaa, O.E. Ogunjinmi, and S.A. Mahmoud, *Discov. Mater.*, **5**(2025):274. https://doi.org/10.1007/s43939-025-00414-4

[57] O.C. Olatunde, D.C. Onwudiwe, and S. Makgato, *Results Chem.*, **17** (2025):102611. https://doi.org/10.1016/j.rechem.2025.102611

[58] L. Zhang, T. Xu, X. Zhao, and Y. Zhu. *Appl. Catal. B*, **98**(2010):138-146. https://doi.org/10.1016/j.apcatb.2010.05.022

[59] G. Greczynski, and L. Hultman. *Sci. Rep.*, **11**(2021):11195. https://doi.org/10.1038/s41598-021-90780-9

[60] G. Greczynski, and L. Hultman. *ChemPhysChem*, **18**(2017):1507-1512. https://doi.org/10.1002/cphc.201700126

[61] A.D. Vishwanath, J.S. Shankar, N.M. Eknath, A.A. Eknath, and K.N. Haribhau. *Orient. J. Chem.*, **32**(2016):933-940. http://dx.doi.org/10.13005/ojc/320219

[62] P. Kaur, Kriti, Rahul, S. Chalotra, H. Kaur, A. Kandasami, and D.P. Singh. *Appl. Surf. Sci. Adv.*, **5**(2021):100100. https://doi.org/10.1016/j.apsadv.2021.100100

[63] M. Agarwal, S.K. Garg, K. Asokan, D. Kanjilal, and P. Kumar. *RSC Adv.*, **7**(2017):13836–13845. https://doi.org/10.1039/c6ra25237k

[64] Q. Liu, Y. Liu, C. Li, J. Li, H. He, Y. Li, and W. Li. *J. Mater. Sci.: Mater. Electron.*, **28**(2017):4004–4013. https://doi.org/10.1007/s10854-016-6013-0

[65] Z. Tian, Y. Zeng, H. Zhao, J. Yang, and H. Zhang. *Catal. Commun.*, **177**(2023):106665. https://doi.org/10.1016/j.catcom.2023.106665

[66] H.N. Tran, S. Park, F.T.A. Wibowo, N.V. Krishna, J.H. Kang, J.H. Seo, H. Nguyen-Phu, S.Y. Jang, and S. Cho. *Adv. Sci.*, **7**(2020):2002395. https://doi.org/10.1002/advs.202002395

[67] X. Liu, J. Gao, Y. Chen, C. Li, J. Chen, W. Qu, X. Chen, Z. Ma, and X. Tang. *ChemCatChem*, **10**(2018):3999– 4003. https://doi.org/10.1002/cctc.201800818

[68] B.K.Shukla, S. Rawat, M.K. Gautam, H. Bhandari, S. Garg, and J. Singh. *Molecules*, **27**(2022):2309. https://doi.org/10.3390/molecules27072309

[69] L. Cheng, L. Liu, D. Wang, F. Yang, and J. Ye. *J. of CO_2 Util.*, **29**(2019):196–204. https://doi.org/10.1016/j.jcou.2018.12.013

[70] X. Meng, and Z. Zhang. *Appl. Surf. Sci.*, **392**(2017):169-180. https://doi.org/10.1016/j.apsusc.2016.08.113

[71] N.A. Morozov, O.Yu. Sinelshchikova, N.V. Besprozvannykh, and T.P. Maslennikova. *Russ. J. Inorg. Chem.*, **65**(2020):1127–1134. https://doi.org/10.1134/S0036023620080124

[72] W. Kong, H. Jiang, X. Chen, B. Chen, H. Wang, Z. Shi, L. Chen, J. Wen, P. He, J. Wu, and J. Lin. *J. Taiwan Inst. Chem. Eng.*, **181**(2026):106515. https://doi.org/10.1016/j.jtice.2025.106515

[73] Y. Sun, J. Wu, T. Ma, P. Wang, C. Cui, and D. Ma, *Appl. Surf. Sci.*, **403** (2017):141–150. http://dx.doi.org/10.1016/j.apsusc.2017.01.130

[74] S. Chang, F. Li, Y. Cai, and Y. Shen. *Digest J. Nanomater. Biostruct.*, **13**(2018):369-374.

[75] T. Chankhanittha, B. Johnson, R.J. Bushby, T. Butburee, P. Khemthong, and S. Nanan. *J. Alloy. Compds.*, **1008**(2024):176764. https://doi.org/10.1016/j.jallcom.2024.176764

[76] M. Xiao, M. Li, Y. Lun, Q. Pan, B. Ai, and J. Xiong. *J. Nanomater.*, **2021**(2021)8955548. https://doi.org/10.1155/2021/8955548

[77] Z.X. Dai, L.Y. Zhang, C.L. Ruan, Z.Q. Yun and G.H. Zheng. *Digest J. Nanomater. Biostruct.*, **17**(2022):179-191. https://doi.org/10.15251/DJNB.2022.171.179

[78] Phuruangrat, S. Buapoon, T. Bunluesak, P. Suebsom, S. Wannapop, T. Thongtem, and S. Thongtem. *Solid State Sci.*, **128**(2022):106881. https://doi.org/10.1016/j.solidstatesciences.2022.106881

[79] T. Zhou, D. Xu, M.g Lu, P. Wang, J. Zhu. *Res. Chem. Intermed.*, **44**(2018):6431–6444. https://doi.org/10.1007/s11164-018-3499-5

[80] X.Q. Feng, M. Zhou, Y. Du, J.Y. Cai, J.Y. Bi, J.Y. Wang, Y.D. Wang, and X.F. Li. *Russ. J. Inorg. Chem.*, **70**(2025):306–318. https://doi.org/10.1134/S0036023624603118

[81] H.T. Nguyen, V.D. Doan, T.L.H. Nguyen, A.T. Nguyen, Q.H. Tran, V.A. Tran, and V.T. Le. *RSC Adv.*, **15**(2025):6241–6259. https://doi.org/10.1039/d5ra00625b

[82] F. Elgharbi, F. Baragh, T. Hu, J.S.M. Quimbayo, R. Brahmi, A. Heponiemi, and M. Agunaou. *Surf. Interf.*, **80**(2026):108370. https://doi.org/10.1016/j.surfin.2025.108370

[83] T.K.M.P. Kumar, and S.K.A. Kumar. *Photochem. Photobiol. Sci.*, **18**(2019):148-154. https://doi.org/10.1039/C8PP00330K

[84] J. Li, F. Yang, Q. Zhou, R. Ren, L. Wu, and Y. Lv. *J. Colloid Interf. Sci.*, **546**(2019):139-151. https://doi.org/10.1016/j.jcis.2019.03.028

[85] J. Yang, H. Zhu, Y. Peng, P. Li, S. Chen, B.g Yang, and J. Zhang. *Nanomaterials*, **10**(2020):756. http://dx.doi.org/10.3390/nano10040756

[86] D. Wang, Y. Zhu, J. Li, W. Yang, Y. Zhao, and G. Chen. *Colloids Surf. A*, **727**(2025):138136. https://doi.org/10.1016/j.colsurfa.2025.138136

[87] Mancuso, S. Mottola, O. Sacco, V. Vaiano, and I.D. Marco. Nanomaterials, 13(2023):3130. https://doi.org/10.3390/nano13243130

[88] A.A. Rasheed-Adeleke, N.H. Seheri, O.A. Oyewo, S.S. Makgato, H. Ferjani, and D.C. Onwudiwe. Appl. Phys. A, 131(2025):857. https://doi.org/10.1007/s00339-025-08960-7

[89] Salaeh, A. Phuruangrat, A. Somdee, T. Thongtem, and S. Thongtem. Iran. J. Catal., 15(2025):152520. https://doi.org/10.57647/j.ijc.2025.1502.20

[90] Salaeh, A. Phuruangrat, A. Somdee, T. Thongtem, and S. Thongtem. Russ. J. Phys. Chem. A, 99(2025):2159–2170. https://doi.org/10.1134/S0036024425701614

[91] M. Tomar, C. Bosch, J. Everaert, R. Bhimpuria, A. Thapper, A. Orthaber, and K.E. Borbas. Org. Lett., 26(2024):10752−10756. https://doi.org/10.1021/acs.orglett.4c03723

`